Circularly polarized narrowband terahertz radiation from a eulytite oxide by a pair of femtosecond laser pulses

R. Takeda, N. Kida,* M. Sotome, Y. Matsui, and H. Okamoto
Department of Advanced Materials Science, The University of Tokyo, 5-1-5 Kashiwa-no-ha, Chiba 277-8561, Japan
(Received 30 December 2013; published 17 March 2014)

We report on terahertz radiation induced by an optical rectification process in a noncentrosymmetric and insulating oxide, eulytite $Bi_4Ge_3O_{12}$, at room temperature. The radiated terahertz pulse consists mainly of a temporal oscillation component with a frequency of 2.01 THz. The generation of this oscillation is ascribed to an increase in the effective generation length for the terahertz radiation up to about 2 mm at 2.01 THz. By using a pair of femtosecond laser pulses with an appropriate interval, polarization, and power, we succeeded in controlling the trajectory of the radiated terahertz wave. This method also enabled us to generate circularly polarized narrowband terahertz radiation with 2.01 THz.

DOI: 10.1103/PhysRevA.89.033832 PACS number(s): 42.65.Re, 77.84.−s, 42.70.Mp, 42.72.Ai

I. INTRODUCTION

Recent developments in terahertz science and technology have provided the possibility for the applications of terahertz waves to various kinds of imaging, sensing, and spectroscopy [1]. In this context, a challenging subject is to generate and control circularly polarized terahertz radiation. It would improve the performance of terahertz applications and open up a new opportunity to reveal the nature of light-matter interaction in solids. For example, it is known that strong absorptions of magnetic excitations induced by chirality in magnets [2] and of the vibration modes of the chiral structures in DNA emerge in the terahertz frequency region [3]. These collective modes would show unique optical properties such as circular dichroism in the terahertz frequency region, i.e., the different optical response between clockwise and anticlockwise circularly polarized terahertz waves. Thus, a high-quality circularly polarized terahertz wave is expected to be used for advanced spectroscopic studies of solids with chirality in the terahertz frequency region.

To control the polarization state of a linearly polarized terahertz wave, terahertz optical components such as polarizers, wave plates, and filters, have been investigated using, for example, semiconductors [4,5], metamaterials [6–11], carbon nanotubes [12,13], and insulators [14–17]. As for a circularly or elliptically polarized terahertz wave, it was demonstrated that a linearly polarized terahertz wave becomes elliptic with an ellipticity of ∼0.5 passing through the chiral metamaterials such as chiral metal screw arrays [7] and chiral molecules [11]. In birefringent medias such as quartz [14–16] and $LaAlO_3$ [17], the ellipticity of ∼1.0 [15,17] was achieved by utilizing the uniaxial anisotropy of the refractive index in the terahertz frequency region. Another useful method to obtain a circularly or elliptically polarized terahertz wave is a direct control of the polarization state in a terahertz radiation process of noncentrosymmetric media such as ZnTe by a pair of femtosecond laser pulses with different polarization states [18–21] and by arbitrary shaped femtosecond laser pulses [22]. The generated two terahertz waves can be combined with an arbitrary delay time by adjusting the interval between two femtosecond laser pulses. This results in the polarization-controlled terahertz radiation.

In order to explore a more simple and sophisticated method for the polarization control of the terahertz waves, here, we focus on a noncentrosymmetric and insulating oxide, eulytite $Bi_4Ge_4O_{12}$. $Bi_4Ge_3O_{12}$ has a cubic structure and its point group is T_d ($\bar{4}3m$) [23]. Figures 1(a) and 1(b) show the schematics of the crystal structure [24] and the crystal view of the (110) plane, respectively. $Bi_4Ge_3O_{12}$ has a transparent window from 0.3 to 6 μm [25]. This compound is known as a nonlinear optical crystal with a large second-order nonlinear optical susceptibility [25,26]. It is also used as a constitutive element of x-ray scintillator devices due to its fast photoresponse. Furthermore, $Bi_4Ge_4O_{12}$ is known to have a large electro-optic coefficient (∼0.96 pm/V at 633 nm) in the transparent frequency region [25,26].

In the present paper, we report that a narrowband terahertz wave is radiated from $Bi_4Ge_3O_{12}$ at room temperature via an optical rectification process. We found a prominent temporal oscillation component with a frequency at 2.01 THz in the electric-field wave form of terahertz radiation. On the basis of the comparative optical measurements in the visible and terahertz frequency regions, the generation of the oscillation was ascribed to the increase in the effective generation length up to about 2 mm, which originates from the sharp dispersion of an infrared-active phonon mode at around 2 THz. With the use of a pair of femtosecond laser pulses with an appropriate interval, polarization, and power, we succeeded in controlling the polarization state of terahertz radiation; we obtained circularly polarized narrowband terahertz radiation, the helicity of which was able to be tuned by changing the interval between two femtosecond laser pulses.

II. TENSOR COMPONENTS OF SECOND-ORDER NONLINEAR OPTICAL SUSCEPTIBILITY

Here, we briefly summarize the expression of the second-order nonlinear optical susceptibility dominating the light-induced terahertz radiation. When a noncentrosymmetric medium is irradiated with a femtosecond laser pulse, a dc polarization P is induced via the optical rectification

*Author to whom correspondence should be addressed: kida@k.u-tokyo.ac.jp

 ©2014 American Physical Society

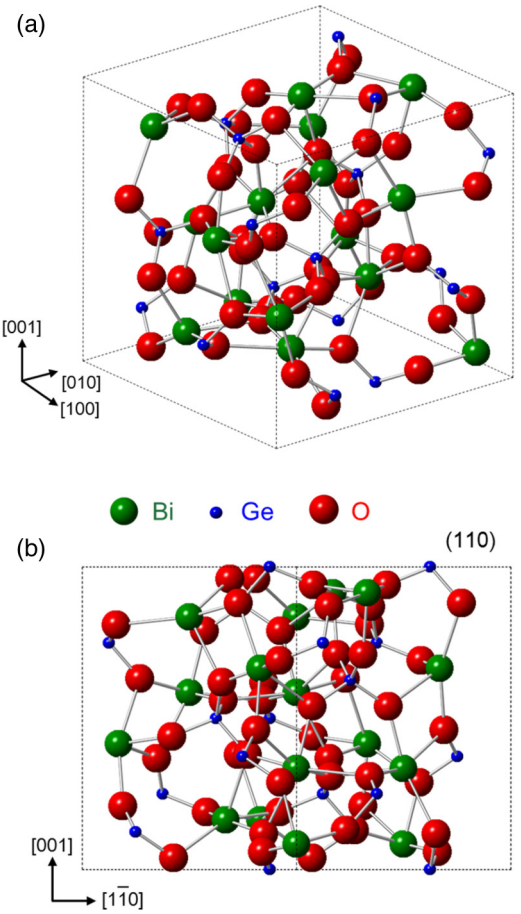

FIG. 1. (Color online) Schematics of the crystal structure of $Bi_4Ge_3O_{12}$ [24]. (a) Crystal structure. (b) Crystal view of (110) plane.

process. Simultaneously, a modulation of P occurs via the difference frequency mixing process, resulting in the terahertz radiation into free space. This process is also considered to be the optical rectification in a broad sense [27], which is recognized as a general terahertz radiation mechanism in noncentrosymmetric media such as ZnTe or GaSe [28,29]. The nonzero tensor components of the second-order nonlinear optical susceptibility $\chi^{(2)}$ of $Bi_4Ge_3O_{12}$ are $\chi_{xyz} = \chi_{yzx} = \chi_{zxy} = \chi_{xzy} = \chi_{yxz} = \chi_{zyx}$ [30]. Here, the x, y, and z axes correspond to the crystallographic principal a, b, and c axes, respectively. Using the contradicted d tensor, the second-order nonlinear polarization $P^{(2)}$ of $Bi_4Ge_3O_{12}$ can be expressed as

$$P^{(2)} = \epsilon_0 \begin{bmatrix} 0 & 0 & 0 & d_{14} & 0 & 0 \\ 0 & 0 & 0 & 0 & d_{14} & 0 \\ 0 & 0 & 0 & 0 & 0 & d_{14} \end{bmatrix} \begin{bmatrix} E_x^2 \\ E_y^2 \\ E_z^2 \\ E_y E_z \\ E_z E_x \\ E_x E_y \end{bmatrix}, \quad (1)$$

where E_x, E_y, and E_z represent the x, y, and z components of the electric field of the femtosecond laser pulse, respectively. ϵ_0 is the dielectric constant in vacuum. We used the laboratory coordinate as the X (horizontal) and Y (vertical) axes [see Fig. 3(a)]. The angle θ was defined as the relative angle between the Y axis and the [001] direction of the crystal. In a (110)-surface crystal [31], the induced $P^{(2)}$ as a function of θ is given by

$$P^{(2)} = \begin{bmatrix} P_{1\bar{1}0} \\ P_{110} \\ P_{001} \end{bmatrix} = \epsilon_0 d_{14} E_0^2 \begin{bmatrix} \sin 2\theta \\ 0 \\ \sin^2 \theta. \end{bmatrix}. \quad (2)$$

E_0 represents the electric field of the femtosecond laser pulses.

III. EXPERIMENTAL DETAILS

Samples of $Bi_4Ge_3O_{12}$ were commercially available (110)-oriented single crystals with a thickness of 1 mm.

For the optical spectroscopy in the terahertz frequency region, we applied two methods. One is the terahertz time-domain spectroscopy in a transmission geometry. Another is the Fourier-transformed infrared (FTIR) spectroscopy in a reflection geometry. In the terahertz time-domain spectroscopy, terahertz waves were obtained from a 0.5-mm-thick (110)-oriented ZnTe crystal by the irradiation of femtosecond laser pulses (the wavelength of 800 nm, the pulse duration of 100 fs, and the repetition rate of 80 MHz) delivered from a mode-lock Ti:sapphire laser. Terahertz waves transmitted across the single crystal were detected by using a standard photoconducting sampling technique with a low-temperature-grown GaAs detector. In the reflection FTIR spectroscopy, the reflectance was measured in the range of 40–600 cm^{-1}. For the optical spectroscopy in the range of 0.5–4.3 eV, we used a grating monochromator equipped with an optical microscope and measured both the reflectance and transmittance spectra of the single crystal.

For the Raman scattering spectroscopy, we used a triple-type monochromator equipped with an optical microscope. A He-Ne laser (633 nm) and a CCD camera were used as an excitation source and a detector, respectively.

In the terahertz radiation experiments, we delivered femtosecond laser pulses to the $Bi_4Ge_3O_{12}$ single crystal. Femtosecond laser pulses of 800 and 1200 nm were generated from a Ti:sapphire regenerative amplifier (the wavelength of 800 nm, the duration of 25 fs, and the repetition rate of 1 kHz) and an optical parametric amplifier pumped by the output of a Ti:sapphire regenerative amplifier, respectively. The electric field of a terahertz pulse radiated from the $Bi_4Ge_3O_{12}$ single crystal was detected in the transmission geometry by a standard electro-optical (EO) sampling technique. For an EO sensor, a 1.0-mm-thick (110)-oriented ZnTe crystal was used. The measurement procedures will be detailed in Sec. IV B. All the experiments including the fundamental optical measurements were performed at room temperature in air.

IV. RESULTS AND DISCUSSIONS

A. Optical spectra

First, we detail the reflectance (R) and transmittance (T) spectra in the visible and terahertz frequency regions (Fig. 2). The R and T spectra in the visible frequency region are shown in Fig. 2(d) by red and black lines, respectively. The sharp decrease in T and the gradual increase in R above ~3.5 eV are attributable to the presence of the strong optical transition

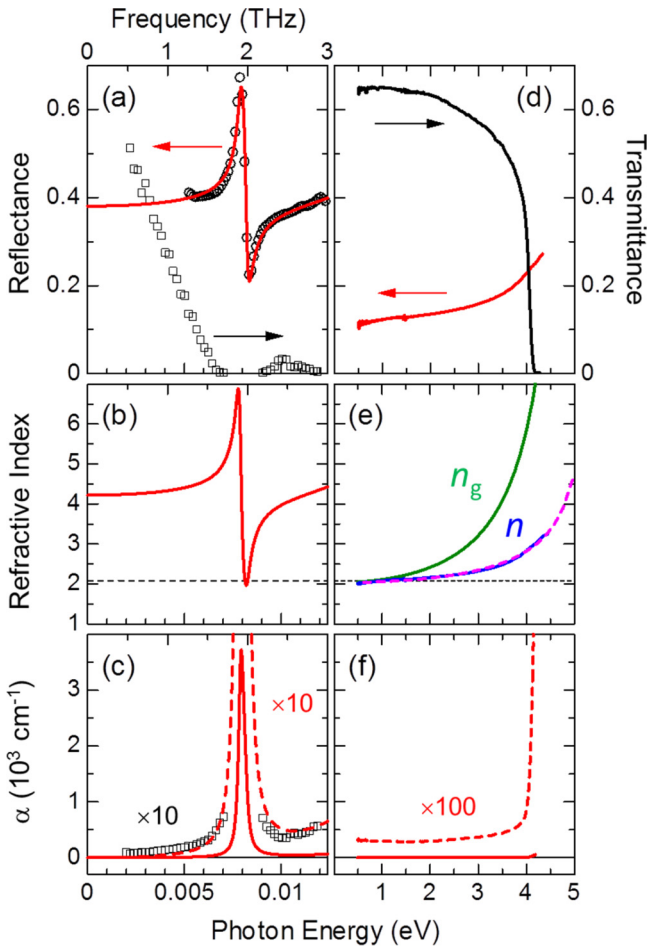

FIG. 2. (Color online) Optical spectra of $Bi_4Ge_3O_{12}$ in the visible and terahertz frequency regions, measured at room temperature. (a) Reflectance (circles) and transmittance (squares) in the terahertz frequency region, measured by the FTIR spectroscopy and terahertz time-domain spectroscopy, respectively. The solid line shows the result of the least-square fit to the data by assuming three Lorentz oscillators (see the Appendix). (b) Refractive index n spectrum as obtained by the dispersion analysis of the measured reflectance spectrum (see the Appendix). (c) Absorption coefficient α spectra obtained by terahertz time-domain spectroscopy (squares) and by the dispersion analysis (solid and broken lines). (d) Reflectance (the red line) and transmittance (the black line) spectra in the visible frequency region, measured by the grating spectroscope. (e) n spectrum (the blue line) as obtained by Kramers-Kronig transformation of the measured reflectance data. The broken line shows the fitting curve by assuming the Sellmeier relationship (see the text). The calculated optical group refractive index n_g spectrum is shown by the green line. The horizontal broken lines in (b) and (g) indicate the value of n_g at 1200 nm (∼2.12). (f) α spectrum obtained from the measured reflectance and transmittance spectra.

across the charge-transfer gap above 4.5 eV. We show in Fig. 2(f) the absorption coefficient α spectrum, which was derived from the R and T data by the relation of $\alpha = -\frac{1}{d}\ln(\frac{T}{(1-R)^2})$, where d is the sample thickness (1 mm). As can be seen, $Bi_4Ge_3O_{12}$ has a transparent window below 4 eV. We also obtained the optical refractive index n spectrum by using the Kramers-Kronig transformation of the R spectrum [the blue line in Fig. 2(e)]. n is nearly constant (∼2) below 2 eV, while it increases to ∼3 near the absorption edge at ∼4 eV. We reproduced the n spectrum as shown by the broken line in Fig. 2(e), which is obtained using the Sellmeier relationship, represented by $n = \sqrt{1 + \frac{S_0\lambda_0^2}{1-(\lambda_0/\lambda)^2}}$ with $S_0 = 5.910\ \mathrm{m}^{-2}$ and $\lambda_0 = 229$ nm, where λ is the wavelength. Using the obtained S_0 and λ_0 values, we calculated the optical group refractive index n_g spectrum. n_g is given by $| n - \lambda\frac{dn}{d\lambda} |$, where n is the optical refractive index. The calculated n_g is shown by the green line in Fig. 2(e). The horizontal broken lines in Figs. 2(b) and 2(e) indicate the value of n_g at 1200 nm (∼2.12).

Figure 2(a) (squares) shows the T spectrum in the terahertz frequency region, which was measured by the terahertz time-domain spectroscopy. The α spectrum deduced from the T spectrum is shown by squares in Fig. 2(c). Due to the strong absorption near 2.01 THz, we yield α only in the frequency range of 0.5–1.7 THz and 2.1–3.0 THz. To evaluate optical constants near 2 THz, we measured the R spectrum by using the FTIR spectrometer, which is shown by circles in Fig. 2(a). There is a clear dispersive structure at around 2 THz. With the use of the dispersion analysis (see the Appendix), we obtained the n and α spectra, as shown by the solid lines in Figs. 2(b) and 2(c), respectively. A sharp peak structure and a clear dispersion can be seen at around 1.9 THz in the α and n spectra, respectively. As shown in Fig. 2(c), the α spectrum thus obtained (the broken line) is almost in agreement with the α spectrum (squares) directly obtained by the terahertz time-domain spectroscopy in the range of 0.5–1.7 THz and 2.1–3.0 THz. We will discuss the origin of this band in Sec. IV C.

B. Terahertz radiation

The experimental setup for the terahertz radiation measurements is schematically shown in Fig. 3(a). The incident femtosecond laser pulse (the electric field E_0) is polarized along the Y axis. The sample was rotated around the propagation direction of the femtosecond laser pulses. The angle of the crystal is expressed by θ, which is the angle of the [001] axis of the crystal relative to the Y axis. Thus, $\theta = 0°$ corresponds to the $E_0 \parallel [001]$-axis, while $\theta = 90°$ corresponds to the $E_0 \parallel [1\bar{1}0]$ axis. By inserting the wire-grid polarizer (WG1) in front of the EO sensor, we measured the vertical component (or equivalently the Y axis component) of the terahertz electric field.

By the irradiation of a femtosecond laser pulse with 1200 nm, we found terahertz radiation from $Bi_4Ge_3O_{12}$. At 1200 nm, $Bi_4Ge_3O_{12}$ is transparent as the penetration depth (∼5.0 mm) [see the α spectrum in Fig. 2(f)] exceeds the thickness of the sample (1 mm) used in this experiment. Figure 3(b) shows a typical example of the electric field of a radiated terahertz wave in time domain when θ was set to be 55°. The laser power was 1.098 mJ/cm^2 per pulse. The electric-field wave form shows a prominent temporal oscillation, which persists over the measured window, i.e., ∼40 ps. We will discuss the origin of the observed oscillation in Sec. IV C.

Figure 3(c) shows the power spectrum of terahertz radiation obtained by the Fourier transformation of the time-domain data shown in Fig. 3(b). The frequency resolution was estimated to be ∼0.012 THz. As can be seen, a sharp resonance is discerned

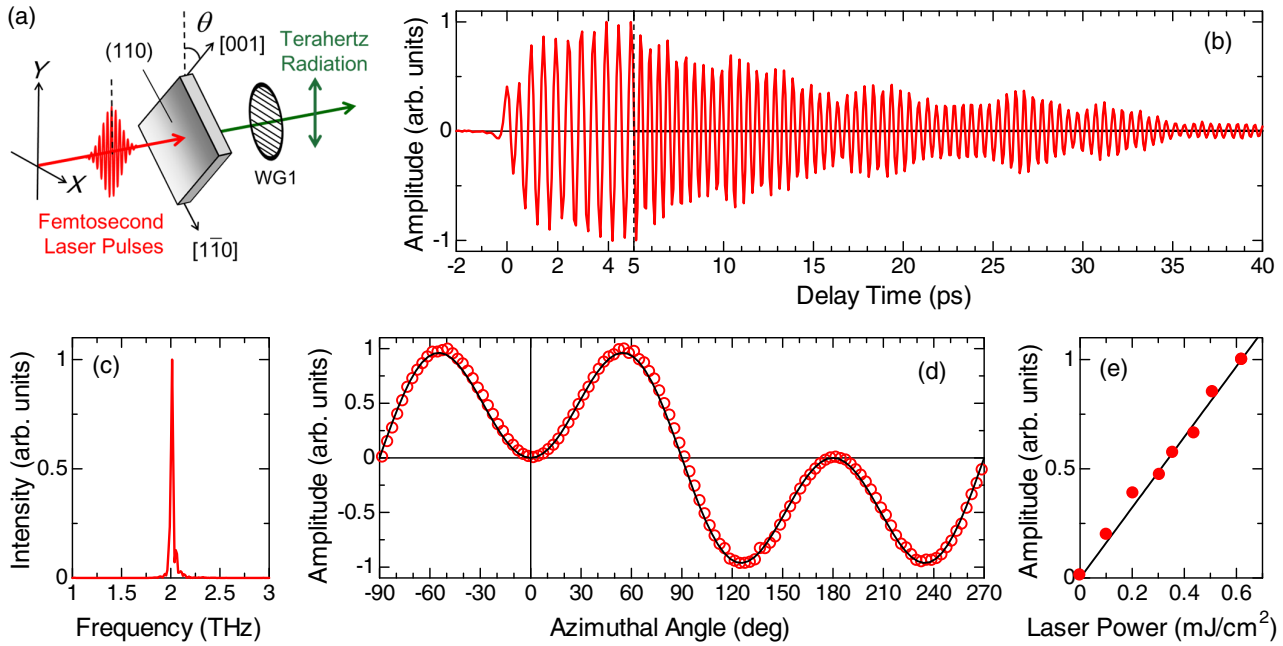

FIG. 3. (Color online) Terahertz radiation from $Bi_4Ge_3O_{12}$ by the irradiation of femtosecond laser pulses, measured at room temperature. (a) Schematic of our experimental setup. We used a (110)-oriented crystal. The electric field of the femtosecond laser pulses was set parallel to the Y axis in the laboratory coordinate. The angle θ was defined as the angle between the Y axis and the [001] axis of the crystal. A wire-grid polarizer (WG1) was inserted to detect the Y axis component of the terahertz wave. (b) The measured time-domain wave form. The wavelength and laser power of femtosecond laser pulses were set to be 1200 nm and 1.098 mJ/cm^2 per pulse, respectively. θ was set to be 55°. (c) The power spectrum of terahertz radiation obtained by Fourier transformation of the time-domain data in (b). We measured the time-domain wave form up to 40 ps at intervals of 0.08 ps [(b)], which corresponds to the frequency resolution of ∼0.012 THz. (d) Azimuthal angle θ and (e) laser power dependencies of the amplitude of terahertz radiation at 0 ps. The solid lines in (d) and (e) show the results of the least-square fit to the amplitude of terahertz radiation using Eq. (3). The laser power was fixed to be 1.098 mJ/cm^2 per pulse [(d)] and θ was fixed to be 55° [(e)].

at 2.01 THz with a full width at half maximum of ∼0.026 THz. As seen in the magnified view shown in Fig. 4(e), besides this peak, a weak shoulder structure at around 1.98 THz, a sharp dip structure at 2.04 THz, and a small peak structure at 2.05 THz are observed. Their origins will also be discussed in Sec. IV C. In the same experimental setup, we also measured terahertz radiation from a 0.5-mm-thick (110)-oriented ZnTe crystal as a reference. The maximum amplitude of the terahertz electric field in $Bi_4Ge_3O_{12}$ was ∼1/50 of that in ZnTe. The real efficiency of the terahertz electric field in $Bi_4Ge_3O_{12}$ is reduced by a factor of 2 by taking into account the sample thickness.

To clarify the mechanism of the observed terahertz radiation, we measured the azimuthal angle dependence of terahertz radiation amplitude E_{THz} at 0 ps. The laser power was set to be 1.098 mJ/cm^2 per pulse. The measured E_{THz} as a function of θ are shown by open circles in Fig. 3(d). The absolute value of E_{THz} reaches the maxima at −55°, 55°, 125°, and 235°. The phase of E_{THz} is reversed by rotating the sample by 180°. Furthermore, E_{THz} becomes zero at −90°, 0°, 90°, 180°, and 270°. When we assume a terahertz radiation by the optical rectification mechanism discussed in Sec. II, the amplitude of terahertz radiation E_{THz} in the experimental setup shown in Fig. 3(a) is given by the following formula:

$$E_{THz} \propto \epsilon_0 d_{14} E_0^2 \sin^2\theta \cos\theta. \quad (3)$$

The observed θ dependence of E_{THz} can be well reproduced by Eq. (3) as shown by a solid line in Fig. 3(d). Furthermore, according to Eq. (3), E_{THz} should be proportional to the laser power (E_0^2) of the incident femtosecond laser pulses. To ascertain this, we measured the laser power dependence of E_{THz}. θ was set to be 55°. The result is shown by solid circles in Fig. 3(e). E_{THz} linearly depends on the laser power, as indicated by the solid line. Thus, from the azimuthal angle and laser power dependencies, we conclude that the mechanism of terahertz radiation from $Bi_4Ge_3O_{12}$ is the optical rectification process.

C. Origin of narrowband terahertz radiation

Here, we discuss the origin of the observed narrowband terahertz radiation with a frequency of 2.01 THz. In a transparent media, longitudinal-optical (LO) phonon generation via impulsive stimulated Raman scattering (ISRS) process [32] is known to produce the narrowband terahertz radiation, as discussed in semiconductors such as InSb [33] and Li(In,Ga)(S,Se) [34]. To investigate a possibility of the ISRS mechanism as the origin of the present terahertz radiation, we measured the polarized Raman spectra of $Bi_4Ge_3O_{12}$. $Bi_4Ge_3O_{12}$ has 27 Raman active modes ($4A_1 + 9E + 14F_2$) [35]. Raman tensors of F_2 modes have nonzero components in off-diagonal elements. We used the (110) surface of the crystal for the polarized Raman scattering experiments and defined as

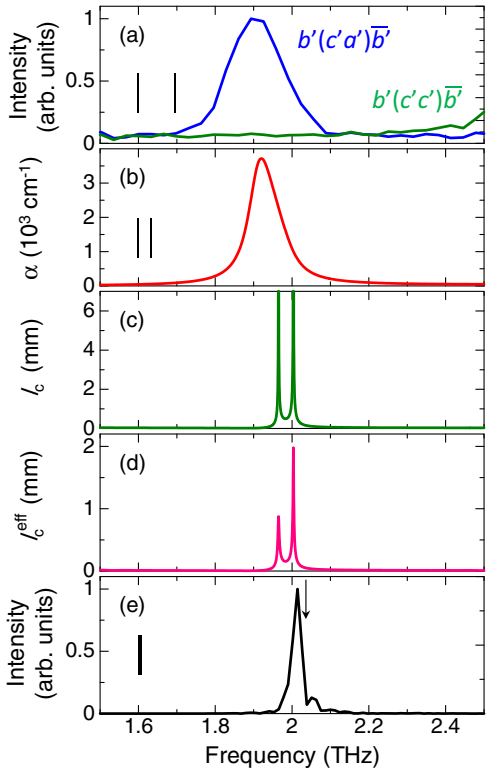

FIG. 4. (Color online) Comparison of optical spectra, coherence length, effective generation length, and power spectrum of terahertz radiation. A pair of vertical lines indicates the frequency resolution. (a) Polarized Raman-scattering spectra, measured using a (110)-oriented crystal, in $b'(c'a')\bar{b}'$ (the blue line) and $b'(c'c')\bar{b}'$ (the green line) configurations. (b) The absorption coefficient α spectrum, as derived from the dispersion analysis of the measured reflectance spectrum shown in Fig. 2(a). (c) Coherence length, calculated by Eq. (7), as a function of frequency. (d) Effective generation length, calculated by Eq. (8), as a function of frequency. (e) Power spectrum of terahertz radiation. An arrow indicates the absorption peak of the water vapor in air.

$a' \parallel [1\bar{1}0]$, $b' \parallel [110]$, and $c' \parallel [001]$. In this case, Raman tensors of F_2 modes are given by

$$F_{2a'} = \begin{bmatrix} 0 & 0 & -f \\ 0 & 0 & f \\ -f & f & 0 \end{bmatrix}, \quad (4)$$

$$F_{2b'} = \begin{bmatrix} 0 & 0 & f \\ 0 & 0 & f \\ f & f & 0 \end{bmatrix}, \quad (5)$$

$$F_{2c'} = \begin{bmatrix} -f & 0 & 0 \\ 0 & f & 0 \\ 0 & 0 & 0 \end{bmatrix}, \quad (6)$$

where f is the constant. Transverse-optical (TO) phonon modes have $F_{2a'}$ and $F_{2c'}$, while the LO phonon mode has $F_{2b'}$. The obtained polarized Raman-scattering spectrum in $b'(c'a')\bar{b}'$ configuration is shown by the blue line in Fig. 4(a). We identify the peak structure at ∼1.9 THz. The full width at half maximum of this band was ∼0.2 THz. The frequency resolution of the experiment was ∼0.1 THz indicated by a pair of vertical lines. On the other hand, this peak structure does not exist in $b'(c'c')\bar{b}'$ configuration [the green line in Fig. 4(a)]. According to the Raman selection rule given in Eqs. (4)–(6), only the F_2 TO phonon mode is active in $b'(c'a')\bar{b}'$ configuration, while the F_2 phonon mode is inactive in $b'(c'c')\bar{b}'$ configuration. Therefore, the observed Raman mode at ∼1.9 THz can be assigned to the F_2 TO phonon mode. Since this mode is also IR active, it is reasonable to consider that the peak structure at ∼1.9 THz observed in the α spectrum [Figs. 2(c) and 4(b)] is also due to this mode. The observed Raman spectrum and the optical selection rules are consistent with the results of the previous report in Ref. [35]. Apparently, the peak position of the F_2 TO phonon mode is different from that of terahertz radiation shown in Fig. 4(e). From these comparative studies of Raman and IR optical spectroscopies, we can exclude the possibility of the ISRS process as the origin of the observed narrowband terahertz wave.

Another candidate of the origin of the narrowband terahertz wave is the increase in the coherence length l_c for the terahertz radiation at the corresponding frequency. l_c is defined as

$$l_c = \frac{\lambda_{THz}}{2|n_g - n_{THz}|}, \quad (7)$$

where λ_{THz} is the terahertz wavelength and n_{THz} is the refractive index in the terahertz frequency range. If the phase-matching condition is satisfied ($n_g = n_{THz}$), l_c can become extremely long, resulting in the enhancement of terahertz radiation. Especially, narrowband terahertz radiation is possible, when the phase-matching condition stands in a narrow frequency region. Such an enhancement of the narrowband terahertz radiation was indeed observed near the phonon-polariton resonance in ZnTe [36].

Now, we can discuss the possibility of the phase-matching-induced narrowband terahertz radiation. With the use of $n_g \sim 2.12$ evaluated at 1200 nm [Fig. 2(e)] and n_{THz} [Fig. 2(b)], we calculated l_c as a function of frequency with a step of 0.0003 THz, which is shown in Fig. 4(c); l_c shows sharp increases at 1.97 and 2.01 THz. This is because the n_g spectrum in the terahertz frequency region has two crossing points with the broken horizontal line of $n_g = 2.12$ as shown in Fig. 2(b). The two frequencies, 1.97 and 2.01 THz, give these crossing points. The peak of terahertz radiation shown in Fig. 4(e) corresponds well to the higher-frequency peak at 2.01 THz in l_c, suggesting that the increase of l_c is responsible for the observed narrowband terahertz radiation. On the other hand, the radiation intensity is not so strong at 1.97 THz giving the lower-frequency peak in l_c, although a shoulder structure is observed at around 1.98 THz in the terahertz radiation [Fig. 4(e)]. As seen in Fig. 4(b), the strong absorption due to the IR-active phonon mode exists at around 1.9 THz and its full width at half maximum is large, being 0.089 THz. Therefore, it is natural to consider that the suppression of terahertz radiation at around 1.97 THz relative to that at 2.01 THz would be due to the reabsorption of terahertz radiation. To ascertain this, we calculated the effective generation length l_c^{eff} including the

absorption effects by using the following formula [37]:

$$l_c^{\mathrm{eff}} = \left(\frac{1 + \exp(-\alpha d) - 2\,\exp\left(-\frac{\alpha}{2}d\right)\cos\left(\frac{\omega}{c}|n_{\mathrm{THz}} - n_g|d\right)}{\left(\frac{\alpha}{2}\right)^2 + \left(\frac{\omega}{c}\right)^2 (n_{\mathrm{THz}} - n_g)^2} \right)^{1/2}, \tag{8}$$

where c is the velocity of light. Figure 4(d) shows l_c^{eff} as a function of frequency with a step of 0.0003 THz. Due to the presence of the absorption peaked at ∼1.9 THz, l_c^{eff} totally decreases and is reduced to ∼2 mm at 2.01 THz and ∼0.89 mm at 1.97 THz. The obtained l_c^{eff} spectrum reproduces not only the presence of two structures (the main peak at 2.01 THz and the shoulder structure at 1.98 THz) in the power spectrum of terahertz radiation [Fig. 4(e)] but also explains qualitatively the relative intensities of those two structures. Thus, we can conclude that the observed narrowband terahertz radiation in $Bi_4Ge_3O_{12}$ is due to the phase matching for the terahertz radiation in a narrow frequency region, which originates from the sharp dispersion of n_{THz} associated with the IR-active phonon mode.

Here, we briefly discuss the reason for the quantitative discrepancy between the spectra of l_c^{eff} and terahertz radiation. The shape of the peak structures in l_c^{eff} is sharp, as compared to that in the spectrum of terahertz radiation. This discrepancy is due to the difference of the frequency resolution; the frequency resolution of the calculated l_c^{eff} is 0.0003 THz, while that of the measured spectrum of terahertz radiation is ∼0.012 THz. Furthermore, in the terahertz radiation experiments, we used the crystal with a thickness of 1 mm, which is close to l_c^{eff} (0.89 mm) at 1.97 THz giving the lower-frequency peak of l_c^{eff}. Therefore, it would be difficult to evaluate precisely the terahertz radiation intensity from the magnitude of l_c^{eff} alone. The dip structure in the power spectrum of terahertz radiation at 2.04 THz indicated by an arrow in Fig. 4(e) is due to the absorption of water vapor in air [38,39]; the absorption located at 2.04 THz is reported by high-resolution Fourier transform far-IR spectroscopy [39]. The small peak structure at 2.05 THz just above the dip might also be related to the absorption of the water vapor, since the presence of a sharp absorption creates an additional intensity in the power spectrum.

From the present systematic optical measurements, we can also show a high potential of $Bi_4Ge_3O_{12}$ as a terahertz emitter. As seen in Figs. 2(b) and 2(c), n shows no dispersion below 1.3 THz, being a nearly constant value of ∼4.2 and α is negligibly small in the same frequency region. Therefore, the phase-matching condition can be achieved [Fig. 2(e)] when the photon energy of the incident femtosecond laser pulse was tuned in to 3.5 eV. Note that α is also very small at 3.5 eV [Fig. 2(f)]. Thus, $Bi_4Ge_3O_{12}$ should be a good candidate for the low-frequency single-cycle terahertz emitter.

V. CHARACTERIZATION OF FIGURE OF MERIT

Here, we estimate the figure of merit (FOM) for the terahertz radiation in $Bi_4Ge_3O_{12}$ at 1200 and 800 nm. Dispersion of the electro-optic coefficient r_{41} has been previously reported from 305 to 633 μm in Ref. [26]. In Ref. [26], dispersion of r_{41} can be reproduced by the polarization-potential model, in which the induced polarization produces the shift of the fundamental absorption edge, resulting in the modification of the Sellmeier relationship. With the use of the fitting parameters given in Ref. [21], r_{41} at 1200 nm yields ∼1.10 pm/V. In the same procedure using reported values of r_{41} from 590 to 690 nm (Ref. [40]), we estimated r_{41} of ZnTe at 1200 nm as ∼3.91 pm/V, which is about four times larger than that of r_{41} of $Bi_4Ge_3O_{12}$ at 1200 nm.

FOM is defined as $2r_{14}n^3/(1+\sqrt{\epsilon})$, where ϵ is the dielectric constant. FOMs of $Bi_4Ge_3O_{12}$ at 1200 and 800 nm were estimated to be ∼3.76 and ∼3.72 with $\epsilon = 16$ [26], respectively, which are about 1/10 of FOMs of ZnTe; ∼39.0 at 1200 nm and ∼39.6 at 800 nm [41].

VI. CIRCULARLY POLARIZED NARROWBAND TERAHERTZ RADIATION

Next, we show that a circularly or elliptically polarized terahertz wave can be obtained in $Bi_4Ge_3O_{12}$ via the combination of two narrowband terahertz waves induced by a pair of the incident femtosecond laser pulses. The experimental setup is illustrated in Fig. 5(a). The similar scheme based upon a double pulse excitation has been reported to control and manipulate the coherent phonon [42,43] and magnon [20,21] excitations located in the terahertz frequency region. We consider the composition of two terahertz wave forms expressed as

$$E_{\mathrm{THz}}(t) \propto \sqrt{\cos^2\omega(t-\tau/2) + \cos^2\omega(t+\tau/2)}, \tag{9}$$

where τ is the delay time between two femtosecond laser pulses. The ellipticity η, which was defined as the ratio of the minimum of $E_{\mathrm{THz}}(t)$ to the maximum of $E_{\mathrm{THz}}(t)$, is represented by

$$\eta = \begin{cases} \tan(\omega\tau/2) & (|\omega\tau| \leqslant \pi/2) \\ 1/\tan(\omega\tau/2) & (|\omega\tau| \geqslant \pi/2). \end{cases} \tag{10}$$

In this experiment, the wavelength of the femtosecond laser pulses was set to be 800 nm. The phase-matching condition of 800 nm is almost identical to that of 1200 nm as the n_g spectrum shows no strong dispersion below 2 eV [Fig. 2(e)]. The pump pulses were split into two pulses (pump A and pump B). Unless otherwise stated, τ was set to be −0.133 ps, which is almost a quarter of the period of the observed narrowband terahertz wave (∼0.5 ps). In this experiment, the angle of the crystal θ was fixed to be 55° [Fig. 5(a)]. According to Eq. (2), E_{THz} is given by

$$E_{\mathrm{THz}} \propto \sqrt{\sin^2 2(\varphi - 55^\circ) + \sin^4(\varphi - 55^\circ)}, \tag{11}$$

as a function of the angle φ, which was defined as the angle between the Y axis and the electric field of femtosecond laser pulses [see Fig. 5(a)]. We show in Fig. 5(b) the calculated E_{THz} as a function of φ. The value of E_{THz} reaches the maxima at −70°, 0°, 110°, and 180°. We also estimated the angle ϕ between the Y axis and the electric field of the radiated terahertz wave [Fig. 5(a)] as a function of φ by the following

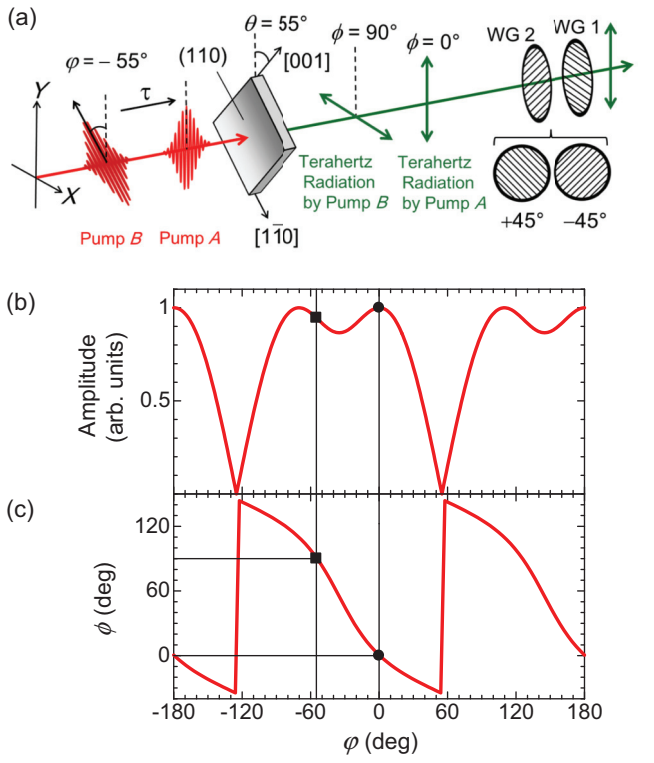

FIG. 5. (Color online) Schematic illustration and theoretical relationship to produce the circularly polarized terahertz radiation. (a) Schematic of experimental setup using a pair of femtosecond laser pulses (the wavelength of 800 nm). The relative delay time τ was the time interval between pumps A and B. θ was fixed to be 55°. The electric fields of pumps A and B were set to be $\varphi = 0°$ and $\varphi = -55°$, respectively. φ was defined as the relative angle of the Y axis in the laboratory coordinate to the electric field of the femtosecond laser pulses. In these cases, the electric fields of the terahertz waves generated by pumps A and B are directed along the Y axis ($\phi = 0°$) and X axis ($\phi = 90°$), respectively [see ϕ as a function of φ shown in (c)]. ϕ was defined as the relative angle of the Y axis to the electric field of the terahertz wave. (b) Amplitude of terahertz radiation as a function of φ. (c) ϕ as a function of φ.

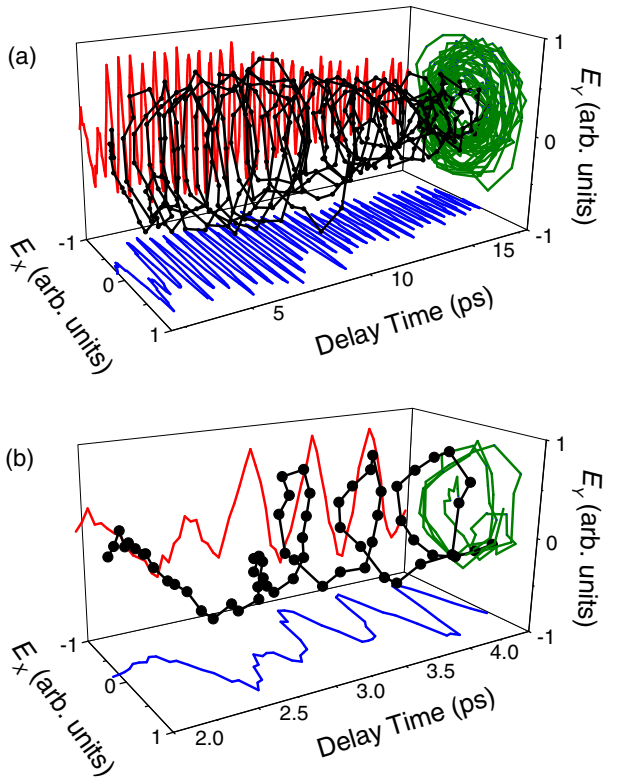

FIG. 6. (Color online) Circularly polarized narrowband terahertz radiation operated at 2.01 THz. (a) Trajectory of the radiated terahertz wave, indicated by the black line. The blue and red lines show the horizontal and vertical components of the measured terahertz wave. The projection of the trajectory of the terahertz wave onto the E_X-E_Y plane is shown by the green line. (b) Magnified view of the trajectory of the terahertz wave.

relationship:

$$\phi = \text{atan}\left(\frac{2}{\tan(\varphi - 55°)}\right) + 55°. \tag{12}$$

Figure 5(c) shows the calculated ϕ as a function of φ. It should be noted that φ is not identical to ϕ, except for the case of $\varphi = 0°$.

A necessary condition to produce the circularly polarized terahertz wave is that the polarization of the radiated terahertz waves generated by pumps A and B should be orthogonal to each other. In our experiments, the electric field of the pump A was set parallel to the Y axis ($\varphi = 0°$) [Fig. 5(a)]. In this condition, the electric field of the radiated terahertz wave generated by pump A was directed along the Y axis [$\phi(0°) \sim 0°$] [Fig. 5(a)], as indicated in Fig. 5(c) by the solid circle. On the other hand, the electric field of pump B was rotated by a half-wave plate and φ was set to be $-55°$ to satisfy the condition of $\phi(-55°) \sim 90°$ as indicated by the solid square in Fig. 5(c). In this case, the electric field of the radiated terahertz wave generated by pump B was directed along the X axis [Fig. 5(a)].

Another necessary condition to produce the circularly polarized terahertz wave is that the magnitude of E_{THz} generated by pumps A and B should be the same as each other. As indicated by the solid circles and squares in Fig. 5(b), the magnitude of E_{THz} at $\varphi = 0°$ and $\varphi = -55°$ is slightly different; the ratio defined as E_{THz} at $\varphi = -55°$ divided by E_{THz} at $\varphi = 0°$, is estimated to be ~0.946. In our experiment, the laser power of pumps A and B were set to be 0.529 mJ/cm^2 per pulse and 0.590 mJ/cm^2 per pulse, respectively, to generate the same magnitude of E_{THz}. The ratio of the laser power ~0.898 is roughly equal to the calculated value.

To determine the polarization state of the radiated terahertz wave, we inserted another wire-grid polarizer (WG2) in front of WG1 [Fig. 5(a)]. We detected $E_{+45°}(t)$ and $E_{-45°}(t)$ components of the terahertz wave by rotating WG2 by ±45° relative to the Y axis. The X and Y components of terahertz radiation can be, respectively, expressed as

$$E_X(t) = E_{+45°}(t) - E_{-45°}(t), \tag{13}$$

$$E_Y(t) = E_{+45°}(t) + E_{-45°}(t). \tag{14}$$

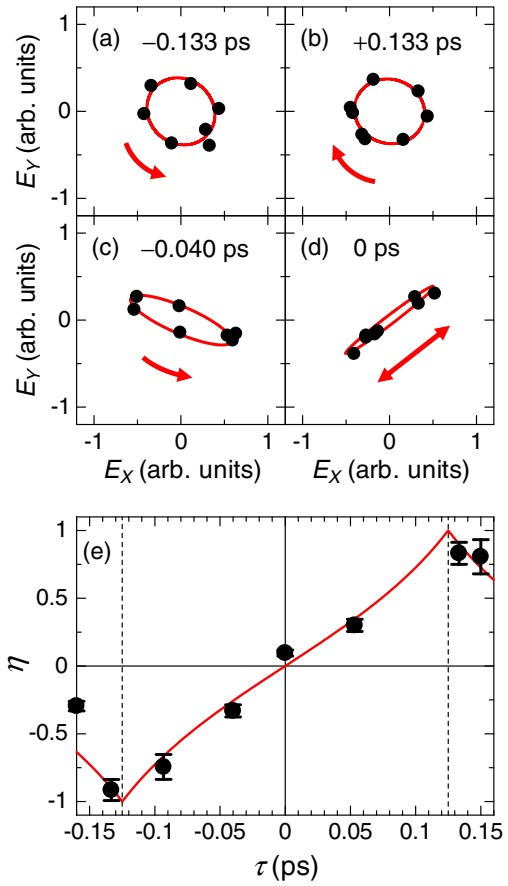

FIG. 7. (Color online) Control of the helicity of circularly polarized narrowband terahertz radiation. The projection of the trajectory of the measured terahertz wave (circles) onto the E_X-E_Y plane as a function of the relative delay time τ between two femtosecond laser pulses; (a) $\tau = -0.133$ ps, (b) $\tau = +0.133$ ps, (c) $\tau = -0.004$ ps, and (d) $\tau = 0$ ps. For convenience, we only show one round of data of the terahertz wave. The solid lines are results of the least-square fit to the data by assuming the ideal ellipse. Arrows represent the rotation direction of the terahertz wave. (e) Ellipticity η as a function of τ (circles) and η is fitted by Eq. (10). The vertical broken lines indicate $\tau = \pm 0.125$ ps, which corresponds to the quarter of the inverse frequency of 2.01 THz.

The obtained $E_X(t)$ and $E_Y(t)$ are shown in Fig. 6(a) by blue and red lines, respectively. A black line represents the three-dimensional trajectory of the radiated terahertz wave obtained by vector compositions of $E_X(t)$ and $E_Y(t)$. For convenience, a projection of the trajectory of the terahertz wave onto the E_X-E_Y plane is shown by the green line. As clearly seen, the circularly polarized narrowband terahertz radiation was achieved in the measured window. The rotation direction was anticlockwise, which can be discerned in the magnified data [Fig. 6(b)]. We show in Fig. 7(a) one round of data (circles), which were extracted from the measured terahertz wave shown in Fig. 6(b). The solid line is a least-square fit to the data by assuming the ideal ellipse. The mean value of η with the standard deviation was evaluated by using six rounds of data. In this procedure, η was estimated to be $\sim 0.91 \pm 0.08$. The arrows indicate the rotation directions of the terahertz waves.

We also measured the trajectory of the terahertz wave as a function of τ. By adjusting τ to 0.133 ps [Fig. 7(b)], the helicity of the terahertz wave was reversed, i.e., clockwise circularly polarized terahertz radiation with $\eta \sim 0.83 \pm 0.08$ was obtained, as expected in Eq. (10). When τ was set to be 0 ps [Fig. 7(d)], the linearly polarized terahertz radiation with η nearly equal to zero ($\sim 0.10 \pm 0.02$) was obtained. For -0.133 ps $< \tau < +0.133$ ps, elliptically polarized terahertz radiation was obtained; a typical example is shown in Fig. 7(c) in which $\tau = -0.040$ ps and $\eta \sim -0.33 \pm 0.04$. Figure 7(e) shows the η values as a function of τ. This τ dependence of η can be well reproduced by Eq. (10), as indicated by the solid line. These results demonstrate that elliptically polarized terahertz waves with arbitrary η values, including a circularly polarized one ($\eta \sim \pm 1$), can be obtained only by changing the interval τ of the incident two femtosecond laser pulses.

VII. SUMMARY

In a noncentrosymmetric and insulating oxide, eulytite $Bi_4Ge_4O_{12}$, we observed strong terahertz radiation by the irradiation of femtosecond laser pulses with 1200 and 800 nm at room temperature. On the basis of the measurements of the azimuthal angle and laser power dependencies, we demonstrated that the terahertz radiation mechanism is the optical rectification induced by the second-order nonlinear optical process. Notably, the temporal oscillation component with a frequency of 2.01 THz emerges in the electric-field wave form and persists up to 40 ps. Based on the systematic investigations of the optical and polarized Raman spectroscopies, we revealed that the observed narrowband terahertz radiation arises from the increase of the effective generation length over 2 mm at 2.01 THz, which originates from the sharp dispersion in the refractive index associated with the IR-active phonon mode at around 2 THz. We also showed that the phase-matching condition would be satisfied below 1.6 THz when the photon energy of the incident femtosecond laser pulses is tuned in to 3.5 eV. This fact suggests that $Bi_4Ge_3O_{12}$ is a good candidate for the low-frequency terahertz emitter.

Moreover, with the use of a pair of femtosecond laser pulses with the appropriate interval, polarization, and power, we achieved circularly polarized narrowband terahertz radiation from $Bi_4Ge_3O_{12}$. We showed that the helicity of terahertz radiation can be controlled only by adjusting the relative delay time between two femtosecond laser pulses. The obtained circularly polarized narrowband terahertz wave is expected to be used as a new light source for a variety of terahertz-wave applications.

ACKNOWLEDGMENTS

We thank A. Doi, J. Fujioka, and Y. Tokura for their support in far-infrared reflectance measurements. This work was partly supported by Sumitomo Foundation and by a Grant-in-Aid by MEXT (Grants No. 25247049, No. 25247058, and No. 25-3372).

APPENDIX: ESTIMATION OF COMPLEX REFRACTIVE INDEX IN TERAHERTZ FREQUENCY REGION

From the measured reflectance R spectrum shown in Fig. 8, we estimated the refractive index n and the absorption

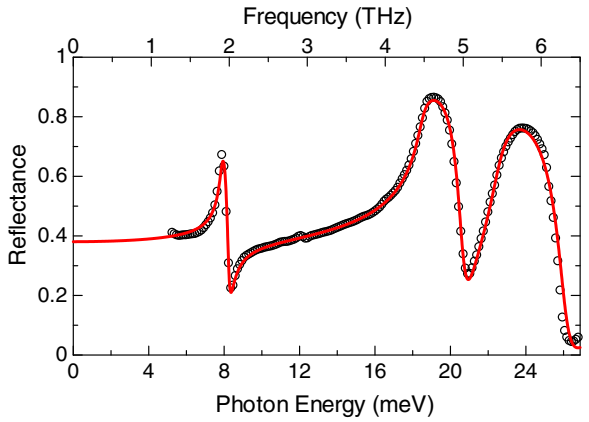

FIG. 8. (Color online) Reflectance spectrum measured by Fourier-transformed infrared spectroscopy. Circles represent the measured reflectance. The solid line indicates the fitting result using Eqs. (A1)–(A3) in the text. The obtained fitting parameters are listed in Table I.

coefficient α spectra by the following procedure. Real $\epsilon_1(\omega)$ and imaginary $\epsilon_2(\omega)$ parts of the dielectric constant, composed of N Lorentz oscillators are, respectively, given by

$$\epsilon_1(\omega) = \epsilon_\infty + \sum_i^N \left[\frac{f_i \omega_i^2 \left(\omega_i^2 - \omega^2\right)}{\left(\omega_i^2 - \omega^2\right)^2 + \gamma_i^2 \omega^2} \right], \tag{A1}$$

$$\epsilon_2(\omega) = \sum_i^N \left[\frac{f_i \omega_i^2 \gamma_i \omega}{\left(\omega_i^2 - \omega^2\right)^2 + \gamma_i^2 \omega^2} \right], \tag{A2}$$

where ϵ_∞, γ_i, ω_i, and f represent the static dielectric constant, the damping coefficient, the central frequency, and the oscillator strength, respectively. Then, R is obtained as

$$R(\omega) = \left| \frac{1 - \sqrt{\{\epsilon_1(\omega) + i\epsilon_2(\omega)\}}}{1 + \sqrt{\{\epsilon_1(\omega) + i\epsilon_2(\omega)\}}} \right|^2. \tag{A3}$$

TABLE I. Obtained fitting parameters with $\epsilon_\infty = 9.685$.

Mode i	ω_i (THz)	γ_i (THz)	f_i
1	1.90	0.064	1.69
2	4.47	0.146	4.85
3	5.45	0.249	1.58

As can be seen in Fig. 8, there are three dispersive structures ($N = 3$). Therefore, we assumed three Lorentz-type modes located at $\omega_1 = 1.90$ THz, $\omega_2 = 4.47$ THz, and $\omega_3 = 5.45$ THz. A least-square fit to the data, using Eqs. (A1)–(A3), is shown by the solid line in Fig. 8. The measured R spectrum can be well reproduced with fitting parameters listed in the Table I. With the use of the calculated $\epsilon_1(\omega)$ and $\epsilon_2(\omega)$, we estimated the n spectrum [Fig. 2(b)] and α spectrum (the red line) [Fig. 2(c)] by using the following relationships:

$$n(\omega) = \sqrt{\frac{+\epsilon_1(\omega) + \sqrt{\epsilon_1(\omega)^2 + \epsilon_2(\omega)^2}}{2}}, \tag{A4}$$

$$\alpha(\omega) = \frac{2\omega}{c} \sqrt{\frac{-\epsilon_1(\omega) + \sqrt{\epsilon_1(\omega)^2 + \epsilon_2(\omega)^2}}{2}}, \tag{A5}$$

where c is the velocity of light. As seen in the magnified α spectrum shown in Fig. 2(c), the α spectrum directly obtained from terahertz time-domain spectroscopy in the transmission geometry is nearly identical to the α spectrum calculated by the procedure described above.

[1] M. Tonouchi, Nat. Photonics **1**, 97 (2007).
[2] S. Bordács, I. Kézsmárki, D. Szaller, L. Demkó, N. Kida, H. Murakawa, Y. Onose, R. Shimano, T. Rõõm, U. Nagel, S. Miyahara, N. Furukawa, and Y. Tokura, Nat. Phys. **8**, 734 (2012).
[3] J. Xu, G. J. Ramian, J. F. Galan, P. G. Savvidis, A. M. Scopats, R. R. Birge, S. J. Allen, and K. W. Plaxco, Astrobiology **3**, 489 (2003).
[4] I. H. Libon, S. Baumgärtner, M. Hempel, N. E. Hecker, J. Feldmann, M. Koch, and P. Dawson, Appl. Phys. Lett. **76**, 2821 (2000).
[5] M. Wagner, M. Helm, M. S. Sherwin, and D. Stehr, Appl. Phys. Lett. **99**, 131109 (2011).
[6] H.-T. Chen, W. J. Padilla, J. M. O. Zide, A. C. Gossard, A. J. Taylor, and R. D. Averitt, Nature (London) **444**, 597 (2006).
[7] F. Miyamaru and M. Hangyo, Appl. Phys. Lett. **89**, 211105 (2006).
[8] N. Kanda, K. Konishi, and M. Kuwata-Gonokami, Opt. Express **15**, 11117 (2007).
[9] H-T. Chen, W. J. Padilla, M. J. Cich, A. K. Azad, R. D. Averitt, and A. J. Taylor, Nat. Photonics **3**, 148 (2009).
[10] X. Lu and X.-C. Zhang, Phys. Rev. Lett. **108**, 123903 (2012).
[11] S. Zhang, J. Zhou, Y.-S. Park, J. Rho, R. Singh, S. Nam, A. K. Azad, H.-T. Chen, X. Yin, A. J. Taylor, and X. Zhang, Nat. Commun. **3**, 942 (2012).
[12] L. Ren, C. Layla, G. Booshehri, W. D. Rice, X. Wang, D. J. Hilton. K. Takeya, I. Kawayama, M. Tonouchi, R. H. Hauge, and J. Kono, Nano Lett. **9**, 2610 (2009).
[13] L. Ren, C. L. Pint, T. Arikawa, K. Takeya, I. Kawayama, M. Tonouchi, R. H. Hauge, and J. Kono, Nano Lett. **12**, 787 (2012).
[14] J.-B. Masson and G. Gallot, Opt. Lett. **31**, 265 (2006).
[15] E. Castro-Camus, J. Lloyd-Hughes, L. Fu, H. H. Tan, C. Jagadish, and M. B. Johnston, Opt. Express **15**, 7047 (2007).
[16] A. K. Kaveev, G. I. Kropotov, E. V. Tsygankova, I. A. Tzibizov, S. D. Ganichev, S. N. Danilov, P. Olbrich, C. Zoth, E. G. Kaveeva, A. I. Zhdanov, A. A. Ivanov, R. Z. Deyanov, and B. Redlich, Appl. Opt. **52**, B60 (2013).
[17] J. Lloyd-Hughes, S. P. P. Jones, E. Castro-Camus, K. I. Doig, and J. L. MacManus-Driscoll, Opt. Lett. **39**, 1121 (2014).
[18] N. Amer, W. C. Hurlbut, B. J. Norton, and Y. Lee, Appl. Phys. Lett. **87**, 221111 (2005).
[19] J. Dai, N. Karpowicz, and X.-C. Zhang, Phys. Rev. Lett. **103**, 023001 (2009).

[20] N. Kanda, T. Higuchi, H. Shimizu, K. Konishi, K. Yoshioka, and M. Kuwata-Gonokami, Nat. Commun. **2**, 362 (2011).
[21] J. Nishitani, T. Nagashima, and M. Hangyo, Phys. Rev. B **85**, 174439 (2012).
[22] M. Sato, T. Higuchi, N. Kanda, K. Konishi, K. Yoshioka, T. Suzuki, K. Misawa, and M. Kuwata-Gonokami, Nat. Photonics **7**, 724 (2013).
[23] R. Nitsche, J. Appl. Phys. **36**, 2358 (1965).
[24] H. Liu and C. Kuo, Z. Krist. **212**, 48 (1997).
[25] D. P. Bortfeld and H. Meier, J. Appl. Phys. **43**, 5110 (1972).
[26] G. Montemezzani, St. Pfändler, and P. Günter, J. Opt. Soc. Am. B **9**, 1110 (1992).
[27] M. Bass, P. A. Franken, J. F. Ward, and G. Weinreich, Phys. Rev. Lett. **9**, 446 (1962).
[28] A. Rice, Y. Jin, F. Ma, and X.-C. Zhang, Appl. Phys. Lett. **64**, 1324 (1994).
[29] A. Nahata, A. S. Weling, and T. F. Heinz, Appl. Phys. Lett. **69**, 2321 (1996).
[30] Y. R. Shen, *The Principles of Nonlinear Optics* (Wiley, New York, 1984).
[31] Q. Chen, M. Tani, Z. Jiang, and X.-C. Zhang, J. Opt. Soc. Am. B **18**, 823 (2001).
[32] Y-X. Yan, E. B. Gamble, and K. A. Nelson, J. Chem. Phys. **83**, 5391 (1985).
[33] M. P. Hasselbeck, L. A. Schlie, and D. Stalnaker, Appl. Phys. Lett. **85**, 173 (2004).
[34] K. Takeya, Y. Takemoto, I. Kawayama, H. Murakami, T. Matsukawa, M. Yoshimura, Y. Mori, and M. Tonouchi, Europhys. Lett. **91**, 20004 (2010).
[35] M. Couzi, J. R. Vignalou, and G. Boulon, Solid State Commun. **20**, 461 (1976).
[36] C. M. Tu, S. A. Ku, W. C. Chu, C. W. Luo, J. C. Chen, and C. C. Chi, J. Appl. Phys. **112**, 093110 (2012).
[37] A. Schneider, M. Neis, M. Stillhart, B. Ruiz, R. U. A. Khan, and P. Günter, J. Opt. Soc. Am. B **23**, 1822 (2006).
[38] M. van Exter, Ch. Fattinger, and D. Grischkowsky, Opt. Lett. **14**, 1128 (1989).
[39] D. M. Slocum, E. J. Slingerland, R. H. Giles, and T. M. Goyette, J. Quant. Spectrosc. Radiat. Transf. **127**, 49 (2013).
[40] T. R. Sliker and J. M. Jost, J. Opt. Soc. Am. **56**, 130 (1966).
[41] Q. Wu and X. C. Zhang, Appl. Phys. Lett. **68**, 1604 (1996).
[42] T. Dekorsy, W. Kutt, T. Pfeifer, and H. Kurz, Europhys. Lett. **23**, 223 (1993).
[43] P. C. M. Planken, I. Brener, M. C. Nuss, M. S. C. Luo, and S. L. Chuang, Phys. Rev. B **48**, 4903 (1993).